Progress in Natural Science: Materials International 29 (2019) 576–581

HOSTED BY

Contents lists available at ScienceDirect

Progress in Natural Science: Materials International

journal homepage: www.elsevier.com/locate/pnsmi

Original Research

Glass-forming ability, phase formation and mechanical properties of glass-forming Cu-Hf-Zr alloys

K. Kosiba[a,*], Kaikai Song[b], U. Kühn[a], Gang Wang[c], S. Pauly[a,**]

[a] Leibniz IFW Dresden, Institute for Complex Materials, D-01069, Dresden, Germany
[b] School of Mechanical, Electrical & Information Engineering, Shandong University (Weihai), 264209, Weihai, China
[c] Laboratory for Microstructures, Institute of Materials, Shanghai University, 200444, Shanghai, China

ARTICLE INFO

Keywords:
Metallic glasses
Glass-forming ability
Composites
Continuous cooling transformation (CCT) diagram
Mechanical properties

ABSTRACT

The influence of Hf additions on the glass-forming ability (GFA), phase formation and mechanical properties of $Cu_{50}Hf_xZr_{50-x}$ (x = 2,5,10,20 at.%) alloys has been systematically investigated. We report on a distinct correlation between phase formation and GFA of $Cu_{50}Zr_{50}$-based alloys. Increasing additions of Hf reduce the thermal stability of the high-temperature B2 Cu(Hf,Zr) phase, while the thermal stability of the corresponding undercooled melt is enhanced. The GFA of these alloy series gradually raises up to 10 at.% Hf, whereas at 20 at.%Hf, the GFA is drastically lowered, since the B2 Cu(Hf,Zr) phase becomes unstable and the precipitation of the low-temperature equilibrium phases is favoured. This interrelation determines the microstructure and results in the formation of Cu-Hf-Zr-based bulk metallic glass composites. These composites not only show appreciable macroscopic plastic strain, but also high yield strength.

1. Introduction

(Bulk) metallic glasses ((B)MGs) are known to exhibit outstandingly high yield strengths (up to 5 GPa) and large elastic limits (about 2%) at ambient conditions [1,2] compared to their crystalline counterparts. Despite these attractive mechanical properties, BMGs are still not used as structural materials in service, so far. The major obstacle is their inherent brittleness, which results from severe strain localization within so-called shear bands [1]. As (B)MGs are plastically deformed, shear bands form and propagate. At the later stages of deformation, shear bands quickly evolve into cracks whose fast propagation ultimately leads to a brittle material failure [1,2].

A very effective way to attenuate the brittle behaviour of (B)MGs is to incorporate crystals into the glass, since crystals hamper the propagation of shear bands and retard failure. The resulting BMG composites can exhibit high strength and plasticity [1–6]. $Cu_{50}Zr_{50}$-based BMG composites are of high interest, since they combine high strength, plasticity and additionally work-hardening [4–7]. They are comprised of the glassy matrix and B2 CuZr crystals, which can undergo a deformation-induced martensitic transformation. The work hardening originates from a martensitic transformation and can overcompensate the work softening of (B)MGs [5–7].

In order to fabricate BMG-composites, the corresponding alloys require a sufficient glass-forming ability (GFA) entailing the formation of a glassy matrix. Compared to multi-component compositions, which can be cast into rods with diameters of more than 10 mm [8], the $Cu_{50}Zr_{50}$ alloy shows a lower GFA. In order to further improve its GFA, different alloying elements are generally added, such as Al [9,10], Ti [11,12], Er [13] and/or Ag [14]. Besides a sufficient GFA, the formation of $Cu_{50}Zr_{50}$-based BMG composites also requires the precipitation of the B2 CuZr phase in the course of melt-quenching. Therefore, the alloying additions have to be chosen in such a way that they do not destabilize the B2 CuZr phase [15] to an extent that it ceases to precipitate [4,6,16,17]. Co is an interesting alloying element in this respect, since, as opposed to the B2 CuZr phase [18], B2 CoZr is stable even at room-temperature [19]. Indeed, previous works have proven that Co additions can stabilize the resulting B2 (Cu,Co)Zr solid solution to room temperatures, but simultaneously deteriorates the GFA of the respective alloys [20,21]. Furthermore, Co-additions tend to lower temperatures at which the martensitic transformation takes place [22], and hence affect the shape-memory behaviour of the B2 CuZr phase.

On the contrary, no B2 phase can be found in the binary Cu–Hf system [23] while all other phases found in the Cu–Zr system are present [18]. Both elements, Hf and Zr, are fully soluble [24] and, hence, Hf is a potential element in order to destabilize the B2 phase to increase the GFA of the resulting alloy. Our motivation is to control the

* Corresponding author.
** Corresponding author.
E-mail addresses: k.kosiba@ifw-dresden.de (K. Kosiba), s.pauly@ifw-dresden.de (S. Pauly).

https://doi.org/10.1016/j.pnsc.2019.08.009
Received 29 January 2019; Received in revised form 5 August 2019; Accepted 13 August 2019
Available online 19 November 2019

composite microstructure by tuning the thermodynamic stability of the B2 phase, which constitutes the phase competing with the vitrification of the melt.

In the present work, Zr is gradually substituted by Hf in order to deliberately vary the temperature region in which the B2 Cu(Hf,Zr) phase is stable. The aim of the current work is to investigate the influence of Hf-additions on the phase formation and GFA of the resulting $Cu_{50}Hf_xZr_{50-x}$ (x = 2, 5, 10, and 20 at.%) alloys. We show here that there is a direct correlation between the phase formation and the GFA, and, furthermore, how this correlation originates from the stability of the B2 Cu(Hf,Zr) phase. The obtained Cu-Hf-Zr-based BMG composites show beneficial mechanical properties.

2. Materials and methods

Pre-alloys of $Cu_{50}Hf_xZr_{50-x}$ (x = 2, 5, 10, and 20 at.%) were prepared from high-purity elements (purity ≥ 99.99%) by arc-melting in a Ti-gettered Ar-atmosphere. Each ingot with a mass of about 25 g was remelted three times to ensure chemical homogeneity. Pieces of the ingots were used to produce ribbons in a single-roller melt-spinning device (Edmund Bühler) also under Ar-atmosphere. Additionally, about 35 mm long rods with a diameter of 2 mm were fabricated via suction casting in a water-cooled copper mould (Bühler MAM1).

Thermal analysis was carried out in a high-temperature differential scanning calorimeter (DSC) (Netzsch 404 C) at a heating rate of 20 K/min to 1373 K in Al_2O_3-crucibles under argon atmosphere. Specimens were heated in a conventional DSC (PerkinElmer Diamond) at a rate of at 40 K/min up to 873 K in Al-crucibles. The glass-transition temperature, T_g, and the crystallization temperature, T_x, were obtained from conventional DSC measurements. The start and end temperatures of the eutectoid transformation (T_{st} and T_{fin}), the solidus temperature T_s and the liquidus temperature T_l were determined from high-temperature DSC measurements of ribbons.

Structural characterization was carried out by X-ray diffraction (XRD) with a STOE STADI P with Mo-$K_{\alpha 1}$ radiation (λ = 0.07093187 nm). Microstructural investigations were conducted using an optical microscope (Zeiss Axiophot, Carl Zeiss AG) and a Zeiss Gemini 1530 scanning electron microscope (SEM) equipped with a Bruker Xflash 4010 spectrometer to conduct energy-dispersive X-ray analysis (EDX).

Compression tests were carried out with an Instron 5869 at a constant strain rate of 1×10^{-4} s^{-1}. A laser-extensometer (Fiedler) was used to directly monitor the strain at the sample surface.

3. Results

3.1. Thermal properties and phase formation

Fig. 1a depicts the XRD pattern of melt-spun $Cu_{50}Hf_xZr_{50-x}$ (x = 2, 5, 10, and 20 at.%) ribbons prepared at a cooling rate of about 10^6 K/s [25]. Only broad maxima are visible and no sharp reflections corresponding to crystalline phase(s) can be observed. In Fig. 1b, the DSC curves further confirm the presence of the amorphous phase in the melt-spun Cu-Hf-Zr-based ribbons. Besides the glass-transition indicated by the glass-transition temperature, T_g, crystallization, which is marked by distinct exothermic peaks (Fig. 1b), sets in at the crystallization temperature, T_x. On further heating, the $Cu_{50}Hf_xZr_{50-x}$ (x = 2, 5, 10 at.%) ribbons exhibit another endothermic event, which indicates the occurrence of the eutectoid transformation of the low-temperature phases, $Cu_{10}Zr_7$ and $CuZr_2$, into the high-temperature B2 CuZr phase [16,17,26–28]. T_{st} and T_{fin} mark the start and end of this transformation, respectively. Interestingly, the DSC trace of $Cu_{50}Hf_{20}Zr_{30}$ does not show the eutectoid transformation. In other words, the B2 CuZr phase does not precipitate before melting begins (T_m). At temperatures above the liquidus temperature, T_l, only the liquid is present. All characteristic temperatures (T_g,T_x, T_{st}, T_{fin}, T_m and T_l) depend on the composition and rise with increasing Hf-additions (Table 1). Particularly, the values of T_{st}, T_{fin}, and T_l are strongly composition-dependent (Table 1). The width of the temperature region in which the B2 phase is stable, ΔT_{B2} (= $T_m - T_{fin}$), diminishes as more Hf is added (Table 1) and this dependence is plotted in Fig. 1c. Above 20 at.% Hf, the B2 phase is not present anymore (Fig. 1b, blue curve). In order to describe the tendency of the B2 CuZr phase to precipitate during quenching of glass-forming CuZr-based melts, the K-parameter has been proposed [17]. This parameter depends on the stability of the liquid, readily characterized by T_l, as well as the competition between the formation of the low-temperature equilibrium phases and the high-temperature B2 CuZr phase. The higher the K-parameter (= T_f/T_l) is, the higher the tendency of a liquid to completely vitrify at a given cooling rate [16,17]. Parameters solely assessing the glass-forming ability (GFA) of alloys were also calculated from the characteristic temperatures [29], namely the reduced glass-transition temperature, T_{rg} (= T_g/T_l) [30] and the γ-parameter (= $T_x/(T_g + T_l)$) [31]. Higher values of both parameters indicate a better GFA. The calculated values of K, T_{rg}, and γ for the $Cu_{50}Hf_xZr_{50-x}$ (x = 2, 5, 10, and 20 at.%) alloy series are listed in Table 1 and illustrated in Fig. 1c. All parameters show the same trend. They increase as more Zr is substituted by Hf up to 10 at.% Hf. When 20 at.%Hf are added to the alloy, the eutectoid transformation is completely suppressed so that the K-parameter cannot be assessed any more. Compared to the $Cu_{50}Hf_x$ Zr_{50-x} (x = 2, 5, and10 at.%) alloys, the GFA of $Cu_{50}Hf_{20}Zr_{30}$severely deteriorates based on the above mentioned GFA-parameters.

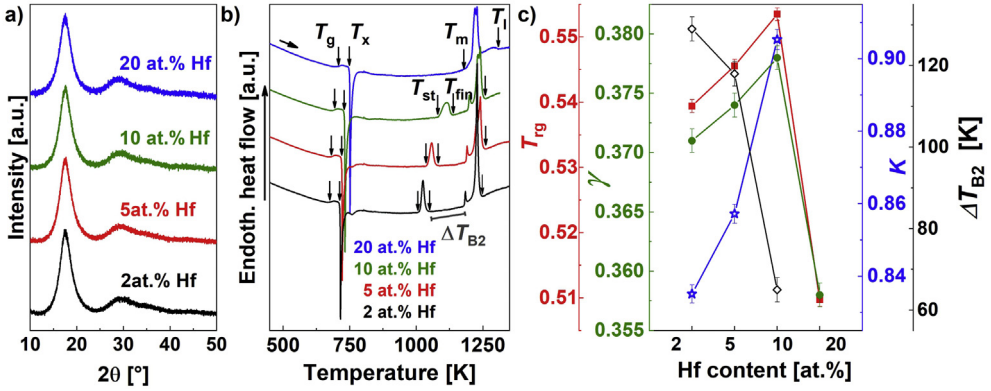

Fig. 1. (a) XRD pattern, and (b) DSC curves of melt-spun ribbons. (c) Thermal parameters assessing the glass-forming ability. For more information the reader is referred to the main text.

Table 1
Characteristic temperatures for the glass-forming $Cu_{50}Zr_{50-x}Hf_x$ (x = 2, 5, 10, 20 at.%) alloy series and the resulting GFA parameters, T_{rg}, γ-, and K-parameter are listed. Typical errors for the determination of T_l are 10 K and for the other temperatures 1 K. All temperatures are given in K.

Alloy (at.%)	T_g	T_x	T_{st}	T_{fin}	T_m	T_l	T_{rg}	γ	K	ΔT_{B2}
$Cu_{50}Zr_{48}Hf_2$	676	715	1107	1046	1175	1253	0.539	0.371	0.835	129
$Cu_{50}Zr_{45}Hf_5$	680	721	1044	1069	1187	1247	0.546	0.374	0.857	118
$Cu_{50}Zr_{40}Hf_{10}$	690	732	1087	1129	1194	1247	0.554	0.378	0.905	65
$Cu_{50}Zr_{30}Hf_{20}$	707	750	–	–	1209	1387	0.510	0.358	–	–

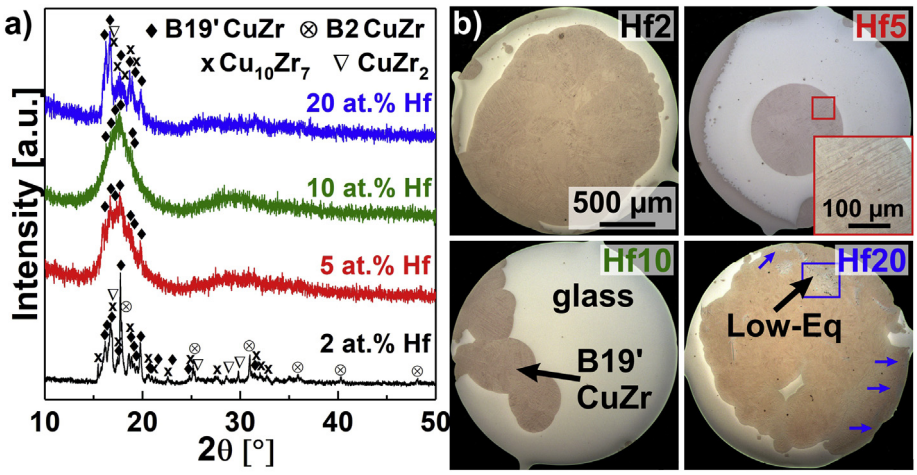

Fig. 2. (a) XRD pattern and (b) Optical micrographs (OM) of as-cast Cu50HfxZr50-x (x = 2, 5, 10, 20 at.%) 2 mm rods (bottom part).

BMG composites were then prepared for the same Cu-Hf-Zr-based alloys via suction casting into a water-cooled copper mould at a distinctly lower cooling rate of about 200 K/s [25]. Fig. 2 depicts their XRD patterns and optical micrographs (OMs). Sharp reflections, which can be allocated to the low-temperature equilibrium phases ($Cu_{10}Zr_7$ and $CuZr_2$), high-temperature B2 CuZr and martensitic B19′ and B33 CuZr phases are visible for the $Cu_{50}Hf_2Zr_{48}$ composite (Fig. 2a). Furthermore, a small volume fraction of an amorphous phase is present (Fig. 2b, brighter phase, DSC curves not shown). As already shown in Fig. 1c, the GFA improves significantly with Hf-additions exceeding 5 at.%. The resulting larger volume fraction of the amorphous phase is reflected in the appendant XRD pattern and OM images. A broad maximum originating from the glassy phase, is superposed by reflections of the martensitic B19′ and B33 CuZr phases. The corresponding optical micrograph (Fig. 2b, Hf5, inset) highlights a lath-like substructure typical of martensite [32]. Further Hf-additions do not change the phase formation of the composite. The XRD pattern of $Cu_{50}Hf_{10}Zr_{40}$ indicates a lower volume fraction of martensite since its reflections are of lower intensity (Fig. 2, Hf10). This observation is consistent with the calculated parameters predicting an improved GFA and accordingly the $Cu_{50}Hf_{20}Zr_{30}$ composite should have a lower volume fraction of the amorphous phase after melt-quenching. The corresponding XRD pattern (Fig. 2a) and optical micrograph (Fig. 2b) also indicate a lower volume fraction of the glass. The intensity of the reflections originating from the crystalline phases is clearly increased compared to the as-cast $Cu_{50}Hf_5Zr_{45}$ and $Cu_{50}Hf_{10}Zr_{40}$alloys (Fig. 2a). In addition to martensite, both low-temperature equilibrium phases ($Cu_{10}Zr_7$ and $CuZr_2$) are present after casting. The optical micrograph shown in Figs. 2b and 3a reveals that the low-temperature equilibrium phases are enshrouded by martensite. In order to verify their formation, an EDX-analysis was conducted and Table 2 lists the composition of the phases depicted in Fig. 3b. The values imply that indeed Cu(Zr,Hf)$_2$, B19' Cu(Zr,Hf), and Cu_{10}(Zr,Hf)$_7$ are present. Consequently, the EDX analysis corroborates the XRD results.

3.2. Mechanical properties of B2 CuZr BMG-composites

In order to investigate the mechanical properties of the as-cast Cu-Hf-Zr-based BMG-composites, cylindrical specimens were uniaxially compressed to fracture. Fig. 4 illustrates the true stress-strain curves of the representative specimens. The characteristic values of all specimens are listed in Table 3. All specimens show a wide range of yield strength, σ_y, fracture strength, σ_f, and especially plastic strain, ε_{pl}, regardless of the Hf-content. Error bars in the compression curves indicate the typical scattering and, therefore, the typical range of values. A vertical bar-chart is shown in the inset of Fig. 4 to exemplify the scattering of ε_{pl}.

4. Discussion

All melt-spun $Cu_{50}Hf_x$ Zr_{50-x} (x = 2, 5, 10, and 20 at.%) ribbons were quenched sufficiently fast so that crystallization was circumvented (Fig. 1a and b) [33]. It has been demonstrated that the melt is quenched at a rate of about 10^6 K/s during melt-spinning [34]. As a result, all melt-spun ribbons are fully amorphous. If the melt is cooled at lower rates, it can partially crystallize prior to vitrification, entailing the formation of BMG composites. All Cu-Hf-Zr alloys were thus also cast into rods. Fig. 2 shows their partially glassy nature.

The phase formation including the crystallization of supercooled liquids depends on the cooling rate [21,35]. In the present case, the solidification behaviour has to be discussed in the following way: On cooling the melt slowly (quasi-equilibrium), the B2 phase precipitates first and transforms into the low-temperature phases, $Cu_{10}Zr_7$ and $CuZr_2$ when the eutectoid temperature is crossed [18]. On intermediate cooling rates, the B2 phase precipitates but is undercooled measurably so that it is present below the eutectoid temperature. From a thermodynamic point of view, the B2 phase is then metastable and the formation of the low-temperature phases is kinetically suppressed [16,17,36,37]. On further increasing cooling rates (up to about 200 K/s), the B2 phase undergoes a thermally induced martensitic transformation to the monoclinic phases B19' CuZr [28] and B33 CuZr [38], as is illustrated using a continuous–cooling–transformation (CCT) diagram

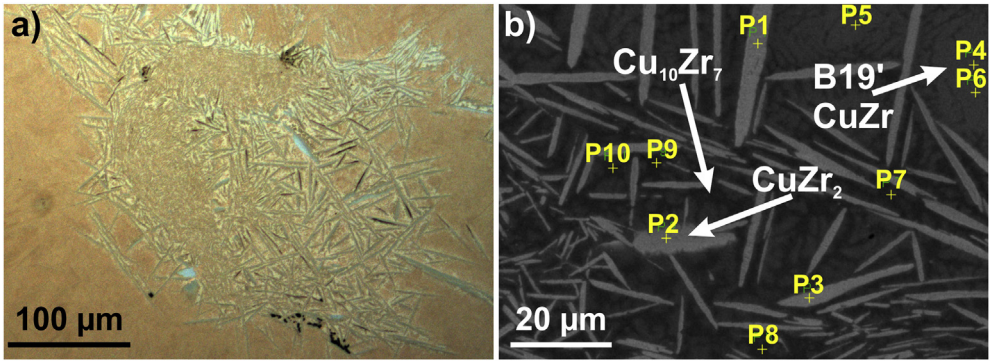

Fig. 3. (a) Optical micrograph, and (b) SEM image including locations used for EDX point analysis (see Table 2).

Table 2
EDX results present the compositions for three different phases of the $Cu_{50}Hf_{20}Zr_{30}$ composite, which are displayed in Fig. 3b. All values are given in at.%, the typical error is about 2 at.%.

Location	Cu	Zr	Hf	Phase
P1	35	38	27	$Cu(Zr,Hf)_2$
P2	36	38	27	
P3	35	37	28	
P4	52	31	17	B19′ CuZr
P5	52	31	18	
P6	50	32	17	
P7	60	27	13	$Cu_{10}(Zr,Hf)_7$
P8	61	26	13	
P9	60	27	14	
P10	61	27	13	

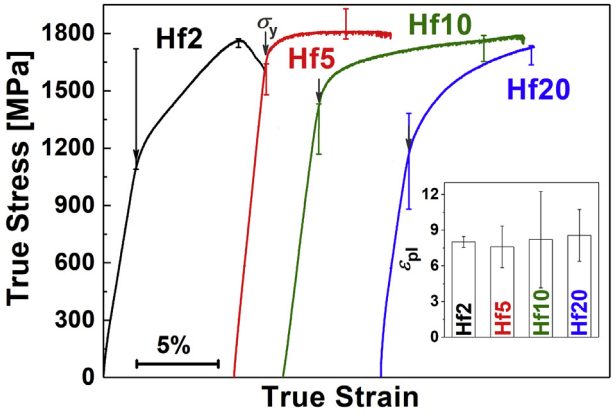

Fig. 4. True stress-strain curves of as-cast $Cu_{50}Hf_xZr_{50-x}$ (x = 2, 5, 10, 20 at.%) 2 mm rods subjected to uniaxial compression. The inset depicts the plastic strain, ε_{pl}, for this alloy series. The average values and deviations, which were obtained from three independent compression tests, are given.

Table 3
Summary of the mechanical properties measured during uniaxial compression for the as-cast $Cu_{50}Zr_{50-x}Hf_x$ (x = 2, 5, 10, 20 at.%) BMG composites. Young's modulus, E, fracture strength, σ_f, and plastic strain, ε_{pl}, are listed.

Sample	E (GPa)	σ_y (MPa)	σ_f (MPa)	ε_{pl} (%)
$Cu_{50}Zr_{48}Hf_2$	85	1654	1755	7.64
	90	1512	1723	7.84
	54	1053	1764	8.51
$Cu_{50}Zr_{45}Hf_5$	77	1467	1941	9.29
	85	1609	1807	7.72
	85	1602	1803	5.77
$Cu_{50}Zr_{40}Hf_{10}$	70	1452	1790	12.50
	61	1260	1656	4.45
	59	1199	1716	7.66
$Cu_{50}Zr_{30}Co_{20}$	71	1363	1647	11.03
	59	1166	1731	7.67
	56	886	1737	6.94

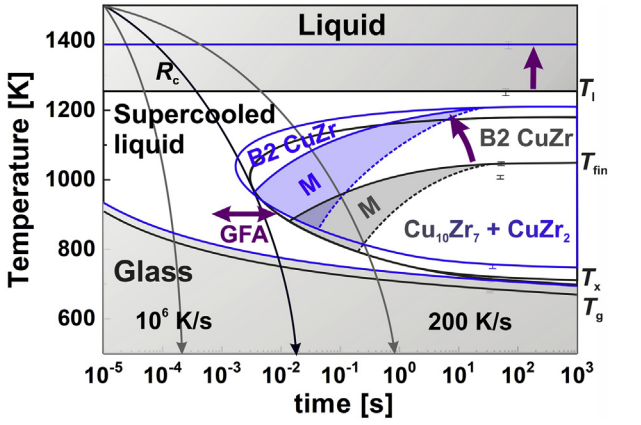

Fig. 5. Continuous-Cooling-Transformation (CCT) diagram of the $Cu_{50}Hf_2Zr_{48}$ (black) and $Cu_{50}Hf_{20}Zr_{30}$ (blue) glass-forming alloys. Cooling rates present at melt-spinning (10^6 K/s), suction casting of 2 mm rods (200 K/s) and near-equilibrium conditions (0.33 K/s) are indicated.

(Fig. 5, both martensitic phases are annotated with “M”). Thereby, B2 CuZr can be partially retained for the $Cu_{50}Hf_2Zr_{48}$ alloy as is also known for $Cu_{50}Zr_{50}$ melt quenched at similar rates [17]. Furthermore, 5 and 10 at.% Hf-additions appear to be sufficient to shift the martensitic transformation temperatures, particularly the martensite finish temperature, to such high values that solely martensite and the glass are obtained after melt-quenching (Figs. 2 and 5).

Owing to the interplay between thermodynamics and kinetics during crystallization of supercooled liquids, the solid-liquid boundary has a “nose”-like shape [39] (Fig. 5). The position of this crystalline nose marks the critical cooling rate, R_c, (slope of black curve in Fig. 5), which is defined as the minimum cooling rate necessary to suppress crystallization or, in other words, to obtain a metallic glass. R_c is shifted to longer times - to the right-hand side of the diagram - for good glass formers (Fig. 5) [39]. Although R_c represents an ideal parameter to quantify the GFA of a melt, it is extremely challenging to measure it accurately [31]. Based on characteristic temperatures, such as T_g, T_x, and T_l, which correlate with R_c, thermal criteria were calculated such as the γ and T_{rg}. They are used as parameters to classify the GFA of alloy systems [29,31,33,40] and allow evaluating the position of the crystalline nose within the CCT-diagram.

For the Cu-Hf-Zr-based alloys, the GFA initially increases when Hf is added up to 10 at.%. Therefore, the crystalline nose is shifted to the

right-hand side of the CCT-diagram (Fig. 1c and Table 1), leading to the decrease of R_c. According to the "confusion principle" [34], an alloy's GFA is enhanced when more components with different atomic sizes are adopted. Then the supercooled liquid is stabilized and in turn crystallization inhibited [34]. Consequently, one would expect a higher GFA when 20 at.% Hf are added to the Cu-Hf-Zr-based system. By contrast, the GFA deteriorates according to γ and T_{rg}, and this trend cannot be explained by the confusion principle, anymore (Fig. 1c and Table 1). Therefore, the deteriorating GFA of $Cu_{50}Hf_{20}Zr_{30}$ is correlated to the competing phase formation during cooling.

As the melts are cooled, either B2 CuZr and/or $Cu_{10}Zr_7$ plus $CuZr_2$ precipitate in the undercooled melt. Alternatively, the supercooled liquid might also vitrify below the glass-transition temperature. All these phases compete with each other [17,20] and, instead of measuring an entire CCT diagram, we use their thermal stability on quasi steady-state heating to get a first idea about the effect of alloy composition on the thermodynamic stability of the respective phases. The high-temperature DSC measurements of the four Cu-Hf-Zr-based alloys (Fig. 1b) reveal that the B2 CuZr phase is destabilized with increasing Hf-additions (Figs. 1 and 5a). Therefore, the time window for its crystallization gradually decreases when the Hf content increases up to 20 at.%. Then, both low-temperature phases crystallize in lieu of the B2 phase directly from the melt. Compared to the quasi steady-state heating, Cu-Hf-Zr-based BMG composites are prepared under non-equilibrium conditions during melt-quenching. The B2 phase and resulting martensitic phases are present at temperatures below the eutectoid temperatures. Their formation is obviously metastable and kinetically favoured over the precipitation of the low-temperature equilibrium phases [36,37]. The B2 phase does not form under quasi steady-state conditions (heating) for the $Cu_{50}Hf_{20}Zr_{30}$ alloy (Fig. 1). Yet, BMG composites comprised of the glass, the equilibrium phases and the B2 phase, which subsequently transforms into the martensitic phases, is obtained by melt-quenching (Fig. 2). Since the B2 phase is thermodynamically not stable, the structure of the $Cu_{50}Hf_{20}Zr_{30}$ supercooled liquid must then resemble the structure of B2 CuZr to a certain extent and the work of Pauly et al. indicates it [41]. There, B2 CuZr nanocrystals precipitate from a $Cu_{50}Zr_{50}$-based glass during its plastic deformation. According to this work, subcritical B2 CuZr nuclei are quenched-in during the preparation of the glass and their growth is then activated as the glass is subsequently deformed. Our results also indicate that the structure of $Cu_{50}Zr_{50}$-based glasses, most likely on a short-range order length scale [41], resembles the structure of B2 CuZr. Furthermore, kinetic constraints seem to be decisive for the growth of these subcritical B2 nuclei. They grow into crystals during melt-quenching, but not during quasi steady-state heating of melt-spun ribbons whose structure should also contain quenched-in subcritical B2 CuZr nuclei [41]. In contrast to melt-quenching where high cooling rates are effective, these subcritical B2 nuclei appear to dissolve during the slow quasi steady-state heating before their growth is activated. Consequently, the thermodynamically stable low-temperature phases crystallize from the $Cu_{50}Hf_{20}Zr_{30}$ supercooled liquid at further heating.

After dwelling on the phase formation under quasi steady-state and non-equilibrium conditions, the focus of the following is on the correlation between the phase formation and the GFA. In general, the GFA of liquids is reflected in the growth rate of crystallizing phases [42,43]. Compared to other intermetallic phases, the B2 CuZr phase has an anomalously low crystal growth rate [42,44]. Intermetallic phases, like NiAl for instance, show relatively high crystal growth rates, since the liquid ahead of the propagating solid-liquid interface is considerably pre-ordered [42]. By contrast, the liquid directly in front of the interface between B2 CuZr crystals and the melt is only poorly structured [42], leading to a lower growth rate and hence a comparatively higher GFA of $Cu_{50}Zr_{50}$-based alloys.

The GFA of the Cu-Hf-Zr-based alloys is enhanced with increasing Hf-content, which also gradually destabilizes the B2 CuZr phase (Fig. 1). Consequently, the B2 phase has less time to crystallize and vitrification is favoured. Amongst the investigated alloys, the GFA is best for $Cu_{50}Hf_{10}Zr_{40}$, but distinctly deteriorates with 20 at.% Hf. As the micrographs (Figs. 2b and 3a) and the EDX analysis of $Cu_{50}Hf_{20}Zr_{30}$ depict (Fig. 3b and Table 2), the $Cu_{10}Zr_7$ and $CuZr_2$ phases crystallized in addition to the martensitic phases. Both low-temperature equilibrium phases are not only present within the cross-section, but also grow from the lateral surface of the rod-specimen (Fig. 2b, blue arrows). Consequently, they do not seem to have formed due to the decomposition of the martensitic phases, but instead due to the direct crystallization from the melt. The liquid structure in front of their solid-liquid interface is then most likely more pre-ordered than that of B2 CuZr. It seems that they involve higher crystal growth rates than the B2 phase. Crystallization is then enhanced and in turn vitrification is less favoured resulting in a lower GFA of the $Cu_{50}Hf_{20}Zr_{30}$ alloy. Thus, the presence of the eutectoid transformation prevents the crystallization of thermodynamically stable phases and, hence, facilitates the vitrification of the supercooled liquid. $Cu_{50}Zr_{50}$-based glass-forming systems should have an optimum GFA when the B2 phase is destabilized as much as possible, but still existent.

Nevertheless, the GFA of all Cu-Hf-Zr-based alloys is sufficiently high to prepare BMG composites and the characterization of their mechanical properties is another aim of the present work. All specimens were subjected to uniaxial compression and Fig. 4 displays the corresponding true stress-strain curves. Despite the large scattering of σ_y, σ_f, and ε_{pl}, a clear trend can be observed. The Cu-Hf-Zr-based specimens with 2 and 20 at.% Hf not only show the largest scattering, but also the lowest yield strength. Furthermore, their work-hardening behaviour is pronounced. It originates from the deformation-induced martensitic transformation of B2 CuZr into B19' and B33 CuZr and the subsequent twinning within the martensite [9,45]. Thereby, the martensitic transformation starts around stress concentration such as, slip bands inside the B2 CuZr crystals or at the interface between the glass and the B2 CuZr crystals. Owing to the mismatch in elastic properties, stress concentrations arise directly at their common interface [45,46].

In general, the volume fraction of the B2 or B19'/B33 CuZr phases strongly affects the yield strength: The higher their crystalline volume fraction, the lower the yield strength of a CuZr-based BMG composite is [1,4,5,47]. Amongst the present alloys, $Cu_{50}Hf_2Zr_{48}$ and $Cu_{50}Hf_{20}Zr_{30}$ have the lowest GFA, leading to the formation of BMG composites with the highest crystalline volume fractions of 58 vol% and 66 vol% at most for $Cu_{50}Hf_2Zr_{48}$ and $Cu_{50}Hf_{20}Zr_{30}$, respectively. The yield strength, σ_y, correlates with the crystalline volume fraction of B2 CuZr BMG composites [5,6,47,48] from both alloys. The composites of both alloys show lowest σ_y of 1000 MPa or even less (Table 3). The perceivable work-hardening behaviour also corroborates the higher crystalline volume fraction [6]. Compared to ε_{pl}, the yield strength scatters significantly for BMG composites with 2 at.%Hf (Fig. 4). They were prepared from the same rod. Since their mechanical behaviour, which strongly depends on the microstructure of the BMG composite [6], varies in such a significant manner, the size and particularly distribution of the crystalline phase must be distinctly non-uniform within a cast rod. This non-uniform composite microstructure origins from the preparation method (melt-quenching). High crystal growth rates and low nucleation rates are accessed during cooling from the melt. Therefore, often only a few and relatively big crystals with a size of up to several 100 µm in diameter (Fig. 2b) crystallize within the supercooled liquid, before it vitrifies [36,37,49].

$Cu_{50}Hf_5Zr_{45}$ and $Cu_{50}Hf_{10}Zr_{40}$BMG composites, which have a better GFA than $Cu_{50}Hf_2Zr_{48}$, show altogether higher σ_y, and the $Cu_{50}Hf_{10}Zr_{40}$ BMG composite has in addition to a high σ_y, also large ε_{pl} up to 12.5%. Owing to the higher glassy volume fraction, their work-hardening is less pronounced (Fig. 4). Moreover, their microstructure shows a higher density of smaller crystals imparting larger plastic deformability. Crystals not only act as obstacles to propagating shear bands resulting in deflection and/or branching [6], but they also provide a larger interface with the glass. Stress concentrations arise at the interface also

serving as fertile sites for the initiation of shear bands [50]. The larger plasticity originates then from the formation of multiple shear bands, their mutual interaction and hindered or even arrested propagation. These results show how strongly the microstructure affects the mechanical behaviour of Cu-Hf-Zr-based BMG composites.

5. Conclusions

The phase formation of the $Cu_{50}Zr_{50}$ system is peculiar, since above the eutectoid temperature the high-temperature B2 CuZr phase is present. We demonstrated that alloying Hf to this binary system allows to shift the eutectoid transformation to higher temperatures. In other words, the B2 Cu(Hf,Zr) phase is thermodynamically destabilized, so that there is gradually less time for the undercooled melt to crystallize into it during melt-quenching. Thus, the competing vitrification is favoured and the GFA of the Cu-Hf-Zr-based alloys is enhanced up to 10 at.% Hf. With an Hf-addition of 20 at.%, the B2 phase is only metastable, while both low-temperature equilibrium $Cu_{10}Zr_7$ and $CuZr_2$ phases are crystallizing directly from the melt. Then, vitrification is less favoured and the GFA of $Cu_{50}Hf_{20}Zr_{30}$ is worse. Hf as alloying element allows to investigate the correlation between the phase formation and extraordinary GFA of the binary $Cu_{50}Zr_{50}$ system as well as enables to understand its origin. By reducing the stability of the B2 phase to a minimum, the GFA of $Cu_{50}Zr_{50}$-based glass-forming alloys can be maximized.

The enhanced GFA of the Cu-Hf-Zr-based alloys entails the preparation of BMG composites. Although all investigated BMG composites show a non-uniform partially crystalline microstructure, their mechanical properties are appreciable: Compressive plastic strain and work-hardening behaviour are detected on a macroscale.

Declaration of interest

The authors declare no competing interests.

Data availability

The raw/processed data required to reproduce these findings cannot be shared at this time due to technical or time limitations.

Acknowledgements

We thank J. Eckert and B. Escher for stimulating discussions. M. Schmidt, S. Donath, B. Bartusch are acknowledged for experimental and technical support. This work was funded by the German Science Foundation under Grants KO 5771/1-1, PA 2275/2–1, PA 2275/4–1 and PA 2275/6–1 and we are also grateful to the Funding from the National Natural Science Foundation of China (51761135125).

Appendix A. Supplementary data

Supplementary data to this article can be found online at https://doi.org/10.1016/j.pnsc.2019.08.009.

References

[1] A.L. Greer, Y.Q. Cheng, E. Ma, Mater. Sci. Eng. R 74 (2013) 71–132.
[2] C.A. Schuh, T.C. Hufnagel, U. Ramamurty, Acta Mater. 55 (2007) 4067–4109.
[3] C.C. Hays, C.P. Kim, W.L. Johnson, Phys. Rev. Lett. 84 (2000) 2901-2901.
[4] Y. Wu, Y. Xiao, G. Chen, C.T. Liu, Z.P. Lu, Adv. Math. 22 (2010) 2770–2773.
[5] F.F. Wu, K.C. Chan, S.S. Jiang, S.H. Chen, G. Wang, Sci. Rep. 4 (2014) 5302-5302.
[6] S. Pauly, G. Liu, G. Wang, U. Kühn, N. Mattern, J. Eckert, Acta Mater. 57 (2009) 5445–5453.
[7] D.C. Hofmann, Science 329 (2010) 1294–1295.
[8] Y.J. Sun, D.D. Qu, Y.J. Huang, K.D. Liss, X.S. Wei, D.W. Xing, J. Shen, Acta Mater. 57 (2009) 1290–1299.
[9] S. Pauly, J. Das, J. Bednarcik, N. Mattern, K. Kim, D. Kim, J. Eckert, Scr. Mater. 60 (2009) 431–434.
[10] B.W. Zhou, X.G. Zhang, W. Zhang, H. Kimura, T. Zhang, A. Makino, A. Inoue, Mater. Trans., JIM 51 (2010) 826–829.
[11] H. Men, S.J. Pang, T. Zhang, Mater. Sci. Eng. A 408 (2005) 326–329.
[12] G.Z. Ma, B.A. Sun, S. Pauly, K.K. Song, U. Kühn, D. Chen, J. Eckert, Mater. Sci. Eng. A 563 (2013) 112–116.
[13] K.K. Song, S. Pauly, B.A. Sun, Y. Zhang, J. Tan, U. Kühn, M. Stoica, J. Eckert, Intermetallics 30 (2012) 132–138.
[14] K.K. Song, S. Pauly, Y. Zhang, B.A. Sun, J. He, G.Z. Ma, U. Kühn, J. Eckert, Mater. Sci. Eng. A 559 (2013) 711–718.
[15] W. Wang, Prog. Mater. Sci. 52 (2007) 540–596.
[16] B. Escher, U. Kühn, J. Eckert, C. Rentenberger, S. Pauly, Mater. Sci. Eng. A 673 (2016) 90–98.
[17] K.K. Song, S. Pauly, Y. Zhang, P. Gargarella, R. Li, N.S. Barekar, U. Kühn, M. Stoica, J. Eckert, Acta Mater. 59 (2011) 6620–6630.
[18] K.J. Zeng, M. Hämäläinen, H.L. Lukas, J. Phase Equilibria Diffusion 15 (1994) 577–586.
[19] W.H. Pechin, D.E. Williams, W.L. Larsen, Trans. ASM 57 (1964) 464–473.
[20] K. Kosiba, P. Gargarella, S. Pauly, U. Kühn, J. Eckert, J. Appl. Phys. 113 (2013) 123505.
[21] S. Pauly, K. Kosiba, P. Gargarella, B. Escher, K.K. Song, G. Wang, U. Kühn, J. Eckert, J. Mater. Sci. Technol. 30 (2014) 584–589.
[22] F.A. Javid, N. Mattern, S. Pauly, J. Eckert, J. Alloy. Comp. 509 (2011) 334–337.
[23] Y. Zhong, A. Saengdeejing, L. Kecskes, B. Klotz, Z.-K. Liu, Acta Mater. 61 (2013) 660–669.
[24] B. Predel, Hf-Zr (Hafnium-Zirconium), in: O. Madelung (Ed.), Ga-Gd – Hf-Zr, Springer Berlin Heidelberg, Berlin, Heidelberg, 1996, pp. 1–4.
[25] R.M. Srivastava, J. Eckert, W. Löser, B.K. Dhindaw, L. Schultz, Mater. Trans., JIM 43 (2002) 1670-1670.
[26] D. Schryvers, Scr. Mater. 36 (1997) 1119–1125.
[27] S.H. Zhou, R.E. Napolitano, Acta Mater. 58 (2010) 2186–2196.
[28] E.M. Carvalho, I.R. Harris, J. Mater. Sci. 15 (1980) 1224–1230.
[29] S. Guo, Z.P. Lu, C.T. Liu, Intermetallics 18 (2010) 883–888.
[30] Z.P. Lu, Y. Li, S.C. Ng, J. Non-Cryst. Solids 270 (2000) 103–114.
[31] Z.P. Lu, C.T. Liu, Acta Mater. 50 (2002) 3501–3512.
[32] W. Pfeiler, Alloy Physics: A Comprehensive Reference, Wiley-VCH Verlag GmbH & Co. KGaA, Weinheim, 2007.
[33] D. Turnbull, Contemp. Phys. 10 (1969) 473–488.
[34] A.L. Greer, Science 267 (1995) 1947–1953.
[35] K. Bräutigam-Matus, G. Altamirano, A. Salinas, A. Flores, F. Goodwin, Metals 8 (2018).
[36] K. Kosiba, S. Pauly, Sci. Rep. 7 (2017) 2151.
[37] K. Kosiba, S. Scudino, U. Kühn, A.L. Greer, J. Eckert, S. Pauly, Acta Mater. 127 (2017) 416–425.
[38] S.H. Zhou, R.E. Napolitano, Scr. Mater. 59 (2008) 1143–1146.
[39] Y.Q. Cheng, E. Ma, Prog. Mater. Sci. 56 (2011) 379–473.
[40] Z.P. Lu, C.T. Liu, Phys. Rev. Lett. 91 (2003) 115505.
[41] S. Pauly, S. Gorantla, G. Wang, U. Kühn, J. Eckert, Nat. Mater. 9 (2010) 473–477.
[42] C. Tang, P. Harrowell, Nat. Mater. 12 (2013) 507.
[43] J. Orava, A.L. Greer, J. Chem. Phys. 140 (2014) 214504.
[44] Q. Wang, L.M. Wang, M.Z. Ma, S. Binder, T. Volkmann, D.M. Herlach, J.S. Wang, Q.G. Xue, Y.J. Tian, R.P. Liu, Phys. Rev. B 83 (2011) 14202.
[45] S.H. Hong, J.T. Kim, H.J. Park, J.Y. Suh, K.R. Lim, Y.S. Na, J.M. Park, K.B. Kim, Intermetallics 62 (2015) 36–42.
[46] S.H. Hong, J.T. Kim, H.J. Park, Y.S. Kim, J.Y. Suh, Y.S. Na, K.R. Lim, J.M. Park, K.B. Kim, Intermetallics 75 (2016) 1–7.
[47] S. Pauly, G. Liu, G. Wang, J. Das, K.B. Kim, U. Kühn, D.H. Kim, J. Eckert, Appl. Phys. Lett. 95 (2009) 101906-101906.
[48] D. Wu, K. Song, C. Cao, R. Li, G. Wang, Y. Wu, F. Wan, F. Ding, Y. Shi, X. Bai, I. Kaban, J. Eckert, Metals 5 (2015) 2134–2147.
[49] A.L. Greer, Metall. Mater. Trans. A 27 (1996) 549–555.
[50] S.H. Hong, J.T. Kim, J.M. Park, G. Song, W.-M. Wang, K.B. Kim, Prog. Nat. Sci. 28 (2018) 704–710.